Towards high resolution resting-state fMRI in the mouse brain

Bárbara Polena Pacheco Araújo Costa
barbara.costa@tecnico.ulisboa.pt

Thesis to obtain the Master of Science Degree in Biomedical Engineering
Supervisors: Dr. Noam Shemesh and Prof. Patrícia Margarida Piedade Figueiredo

Instituto Superior Técnico, Lisboa, Portugal
November 2019

Abstract

Resting-state functional magnetic resonance imaging (rsfMRI) allows the study of functional connectivity in the brain. Through the mapping of functional networks, it is possible to extract information about the intrinsic organization and function of the brain, as well as to study pathologies and arousal states. Considering that controlled preclinical experiments allow combining rsfMRI with other techniques, and that transgenic mouse models are particularly good models for neurological diseases, murine imaging is becoming an attractive option. Still, there are inherent technical difficulties in imaging mice, and detection of robust and consistent networks has been challenging. Moreover, mouse rsfMRI is usually performed at relatively low spatial resolution, limiting the investigation of small structures. In this study, to overcome these shortcomings, rsfMRI datasets were acquired with both standard (0.3 mm x 0.3 mm) and high resolution (0.16 mm x 0.16 mm), different preprocessing pipelines were tested, and a seed-based analysis was conducted with seeds on cortical and subcortical areas. No significant differences were found between pipelines, but it was possible to reproduce functional networks mostly consistent with previous literature, particularly on motor (M1), somatosensory (S1 and S2) and visual (VC) cortices, hippocampus (Hip) and caudate putamen (CPu), for both low- and high-resolution datasets. Considering the high variability of possible data acquisition parameters, anesthetic regimes, preprocessing and analysis pipelines, these consistent network mappings are encouraging results for rsfMRI in mice as translational tools for the study of large-scale neural dynamics, as well as fundamental mechanisms of small structures in the brain.

Keywords: Resting state functional MRI, Functional connectivity, Mouse model, Resting state networks, Seed-based analysis.

Acknowledgement: This document was written and made publicly available as an institutional academic requirement and as a part of the evaluation of the MSc thesis in Biomedical Engineering of the author at Instituto Superior Técnico. The work described herein was performed at the Neuroplasticity and Neural Activity Lab of the Champalimaud Research (Lisbon, Portugal), during the period February-October 2019, under the supervision of Dr. Noam Shemesh. The thesis was co-supervised at Instituto Superior Técnico by Prof. Patrícia Figueiredo.

1. Introduction

Resting-state fMRI (rsfMRI) has been a fast growing technique [1] which can be used to extract information about the inherent organization and function of the brain, as well as to study pathologies [2][3] and arousal states [4]. RsfMRI also allows the mapping of resting state networks (RSNs) (a set of brain regions whose signal shows similarities across time, during rest), which can be observed across species [6][7]. This can be exploited in controlled preclinical experiments through FC modification induced by pharmacological alterations [7], and can also be combined with various techniques such as electrophysiological recordings or optogenetics [8][9]. In this context, the mouse model can especially advantageous, as it allows genetic manipulation, enabling the use of such techniques [10]. Moreover, transgenic mouse models are remarkably good disease models [11][12]. Thus, preclinical experiments in mice are becoming attractive options for a wide range of fMRI resting state studies.

However, rsfMRI is inherently noisy [13] and technically difficult to perform in mice [14], mainly to the brain's very small size. Moreover, although mostly bilateral networks have been found in rodents [15][16], the mapping of these functional networks has been performed under relatively low spatial resolution [17]. These factors limit resting-state fMRI namely when considering the study of potentially interesting small structures, such as the Locus Coeruleus (LC). The LC is a small nucleus deep in the brainstem, considered the center of noradrenergic stimulation in the brain, and thought to be associated with many cognitive

functions such as attention, memory and learning [18]–[20]. Due to its extremely small size, this and other structures could not be directly imaged and subject of focus of resting-state experiments. Hence, there is a need to overcome these shortcomings, as the mapping of functional murine networks with a higher resolution could offer valuable and unique insights on the workings of complex systems based on smaller structures. Thus, the goals of this project included to establish in the lab an MRI protocol suitable for rsfMRI acquisition in mice; to explore urethane anesthesia, to facilitate LC imaging; to establish and optimize a robust preprocessing and analysis pipeline for murine RSN mapping; and to map these networks on standard, i.e. low resolution datasets, to validate the MRI protocol and analysis pipeline, as well as in higher resolution datasets, towards the study of smaller structures.

2. Materials and methods

All aspects of these study were preapproved by the Champalimaud Centre for the Unknown's Ethics Committee operating under Portuguese and EU Law.

2.1. Optimization of acquisition parameters

In this optimization stage, an initial MRI acquisition protocol was established, and rsfMRI datasets were acquired in mice under medetomidine. Urethane anesthesia was characterized, and mice were scanned under urethane.

Animal preparation: A total of 8 female C57BL/6J mice aged between 8 to 10 weeks old were used in these experiments: 5 weighing 25.2 ± 1.4 g for the preliminary medetomidine acquisitions, and 3 weighing 30.4 ± 0.8 g for preliminary urethane acquisitions. Anesthesia was induced with a mixture of air and 5% isoflurane, reduced to 3% for animal preparation, in the case of medetomidine anesthesia. For these acquisitions, medetomidine was administered subcutaneously (0.4 mg/kg bolus, and 0.8 mg/kg/h constant infusion initiated 5-10 minutes after bolus), and isoflurane was kept at 0.5% for the rest of the experiment. For urethane anesthesia, after induction, the animal was injected intraperitoneally with a 1.5 g/kg dosage of urethane as used in previous studies [21]. Isoflurane was discontinued, and an interval of approximately one hour was taken, for the anesthesia to reach full effect. The solution had been previously diluted in saline, and 0.1 mL of solution were injected per 10 g of animal. Once in the bed, the animal's head was secured with a bite bar, ear bars, and a nose cone for continuous gas circulation. A rectal temperature probe and a respiration sensor were placed for real-time monitoring of mouse physiological status, and respiration rates and temperature were monitored and maintained at physiological levels throughout fMRI scanning. Warm water was circulating in a heating pad under the animal, to preserve body temperature, and ophthalmic drops were applied to prevent drying of the cornea. After the medetomidine experiments, medetomidine-antagonist atipamezole was subcutaneously injected, to allow for mice recovery, whereas regarding urethane experiments, the mice were immediately euthanized after the sessions.

MRI protocol: MRI experiments were conducted on a 9.4T horizontal MRI scanner equipped with a gradient system capable of producing up to 660 mT/m in all directions. An 86 mm resonator volume coil was used for transmittance, and a 4-channel array surface cryocoil was used for reception, as it enhances the SNR [22]. Imaging protocol was performed using the software Paravision 6.0.1. After mouse sedation and positioning in the scanner, scout images were acquired in three orthogonal planes to assess the positioning of the brain. After suitable placing of the animal was confirmed, scan adjustments were performed, and a B_0 map was acquired. This map was used for an appropriate shimming in a cylindrical volume covering the brain volume. Structural images were acquired for anatomical reference. Acquisition parameters of the structural image covering the whole brain were: 3D Multiple Gradient Echo (MGE) sequence, Number of averages = 1, Number of echoes = 16, TR = 100 ms, TE = [2.2 : 2.2 : 35.2] ms ([first TE : echo spacing : last TE]), FOV = 18 × 9 × 11.52 mm^3, Data matrix = 180 × 90 × 115. This resulted in an isotropic spatial resolution of 0.1 × 0.1 × 0.1 mm^3, and an acquisition time of 12m16s. After structural acquisitions, a visual stimulation fMRI acquisition was performed, to ensure regular physiological status of the mouse. Standard parameters from previous experiments in the lab were used: GE-EPI sequence, TR = 1000 ms, TE = 12 ms, FOV = 16 × 13.9 mm^2, Data matrix = 100 × 96. This resulted in a spatial resolution of 0.145 × 0.145 mm^2, over 8 slices with a thickness of 0.5 mm, oriented axially. Its acquisition was interleaved, with the order [1 3 5 7 2 4 6 8]. The number of repetitions was 408, and considering that one volume was acquired per second, the acquisition time was 6m48s. The visual stimulation setup and protocol are well established in the lab and were only used for quality control, so they will be briefly described. Succinctly, a fiber-coupled LED with central wavelength located at 470 nm (blue) was used for stimulation. The stimulation paradigm consisted in 5 blocks of 48 seconds rest followed by 24 seconds of visual stimulation. In stimulation periods, the LEDs were flashed bilaterally at a frequency of 2 Hz, with a 10 ms pulse width. After the visual stimulation run, there was an interval, 3 to 5 minutes, during which a quick automatized analysis was run on the Paravision software, to confirm normal BOLD activation on expected areas for visual stimulation in mice. A more robust analysis was performed after the scanning period, for more accurate confirmation. After ensuring the animal physiological status, the resting state acquisitions were started. A tentative protocol was established, with the following parameters: two-shot GE-EPI sequence, TR = 2000 ms, TE = 10.8 ms, FOV = 15.1 × 12.5 mm^2, flip angle = 55°, Data matrix = 116 × 96. The spatial resolution was 0.130 × 0.130 mm^2, over 15 coronally oriented slices. Slice thickness was 0.44 mm, and its acquisition was interleaved. 300 resting state repetitions were acquired, performing a total acquisition time of 10 minutes. Regarding the medetomidine acquisitions, between 2-4 resting state runs were completed for each mouse, per imaging session, with an interval of ~5 minutes between each run. The unbalance of runs between the 5 mice was difficult to avoid since as soon as the animals would start moving or showing signs of

physiological instability, the experiments would be stopped, as this could indicate they would soon wake up. In total, 13 runs were completed. For the urethane acquisitions, a total of 5 runs were acquired. After the resting state acquisitions, if possible, a visual stimulation run was performed, to confirm that the mouse physiology remained stable throughout the session.

Urethane characterization: A total of 7 female C57BL/6J mice, aged between 9 to 10 weeks, were used in these experiments. 2 animals weighing 26.4 ± 1.9 g were tested with a dosage of 1.2 g/kg, and the following 5 mice, weighting 27.6 ± 2.6 g were tested with a dosage of 1.5 g/kg, as previously used in mice resting state experiments [21]. Urethane preparation was carried out identically as described in the previous subsection. Mice were injected intraperitoneally and were then placed in a bed outside the scanner, with warm water circulating below them. Respiratory rates and temperatures were monitored for 3 hours, after which the animals were euthanized.

2.2. Resting state fMRI experiments

In this acquisition phase, a final MRI protocol was established, and rsfMRI datasets were acquired in mice under medetomidine.

Animal preparation: A total of 16 male C57BL/6J mice aged between 7 to 9 weeks old were used in these experiments, weighing 26.7 ± 2.8 g (weight values presented as mean ± standard deviation). All animal preparation was identical to the preliminary medetomidine acquisitions, except the bolus and constant infusion dosages were slightly lower (0.3 mg/kg and 0.6 mg/kg/h, respectively) and after the constant infusion was started, isoflurane was completely discontinued, instead of being kept at 0.5%. These parameters were chosen following previous work [15]. Respiration rates were constant throughout fMRI scanning, ranging between 110 to 160 breaths per minute for all mice, except two mice who exhibited irregular breathing patterns, and woke up before any resting state run could be acquired. Animal body temperature was kept between 36°C and 36.5°C during the rsfMRI acquisitions, as this lower dosage of medetomidine and the lack of any isoflurane rendered the animals more prone to waking up, frequently when temperature rose above these values.

MRI protocol: As in the preliminary experiments, structural images were acquired to be used as anatomical reference. The acquisition parameters of the structural image covering most of the brain (roughly from mid-olfactory bulb to mid-cerebellum) were: RARE sequence, Number of averages = 4, RARE factor = 8, TR = 2200 ms, TE = 9ms, $TE_{effective}$ = 36 ms, FOV = 17 × 11mm^2, Data matrix = 180 × 90 × 115. The spatial resolution was 0.085 × 0.085mm^2 over 25 slices, with a thickness of 0.35 mm. Slices were axially oriented, and its acquisition was interleaved. This resulted in a total acquisition time of 2m20s. Visual stimulation runs were performed in the beginning, and if possible, at the end of the session, identically as described for the preliminary runs. After ensuring animal physiological stability, the resting state acquisitions were started. A protocol was established based on [15], with the following parameters: single-shot GE-EPI sequence, TR = 2000 ms, TE = 15 ms, FOV = 20 × 20 mm^2, flip angle = 75°, Data matrix = 64 × 64. The spatial resolution was 0.3125 × 0.3125 mm^2, over 17 axially oriented slices, covering brain areas from the end to the olfactory bulb to the beginning of the cerebellum. Slice thickness was 0.5mm, and its acquisition was interleaved. 300 resting state repetitions were acquired, performing a total acquisition time of 10 minutes. Another protocol was established, for a higher resolution acquisition, with identical parameters, except: FOV = 15 × 15mm^2, Data matrix = 90 × 90, resulting in a spatial resolution of 0.167 × 0.167 mm^2, but with the same acquisition time. Between 2 to 3 lower resolution resting state runs were completed for each mouse, with an interval of ~5 minutes between each run, except for the two mice that woke up before any resting state acquisition could be completed. In total, 30 low-resolution runs, and 10 high-resolution runs were completed. After the resting state acquisitions, if possible, a visual stimulation run was performed.

2.3. Data analysis

The visual stimulation runs were analyzed using the Statistical Parametric Mapping (SPM) package [23] (SPM12, Wellcome Trust Centre for Neuroimaging, London, UK) for MATLAB, and a Graphical User Interface (GUI) named fmRAT [24], which provided a simple and efficient pipeline for these standard fMRI acquisitions. All these steps are well-established and common practice in this lab and considering that they are only used for quality control, they will be succinctly described: The individual datasets were motion corrected, smoothed with a 3D Gaussian Filter with a FWHM of 0.2 mm, after which the data was fit in a General Linear Model (GLM). The activation maps were thresholded at a p-value $p < 0.01$ and clusters with less than 15 voxels were removed.
The resting state runs were analyzed using FSL (FMRIB Software Library, v5.0.11, www.fmrib.ox.ac.uk/fsl), AFNI (ver 17.2.05, National Institutes of Health, USA), ANTS [25] (v2.3.1, http://stnava.github.io/ANTs/), and Nipype [26] software Nibabel (https://github.com/nipy/nibabel) and Nilearn (http://nilearn.github.io/), as well as Python 3.0 functions in the SciPy ecosystem [27].

Preprocessing: Regarding functional runs, after raw data quality was ensured, a motion and slice timing correction algorithm was applied [28]. The motion parameters were stored to be later used as regressors. Afterwards, a mean image was computed, and a brain mask was automatically created. After individual inspection of the functional brain masks, an outlier detection algorithm was applied on the masked data. If a volume had a displacement larger than 0.3 mm, in relation to the mean image, or a mean intensity image deviating more than 3 standard deviations from the mean, it was detected as an outlier. Only runs with less than 4 outliers (≤ 1%) were further processed. A nuisance removal step was then performed, and it included motion parameter and outlier regression. Bandpass filtering was also applied, with cut-off frequencies of 0.01 Hz and 0.2 Hz. This was the “baseline” nuisance removal, but two variants of this step were also performed, one including a

Global Signal Regression (GSR), and another using a timeseries representing CSF as a regressor. For this step, ventricular masks were manually delineated for all functional runs. The preprocessed functional images were then registered onto the structural space, using a rigid transformation, followed by a non-linear transformation. The structural images were registered onto an atlas – the C57BL/6J model of the Australian Mouse Brain Mapping Consortium [29], using a rigid, followed by an affine, and lastly a non-linear transformation. After registration, a 2-D spatial smoothing using a Gaussian kernel with a FWHM = pixel size (0.3125 and 0.167 for the low- and high-resolution runs, respectively) was applied.

Postprocessing: After the preprocessed data is in the same space, a seed-based analysis was carried out. The seeds were manually defined from labelled regions on the atlas. They were drawn in the left hemisphere of the following regions: Caudate putamen (CPu), Hippocampus (Hip), Primary motor cortex (M1), Primary (S1) and Secondary (S2) somatosensory cortex, Thalamus (Thal) and Visual Cortices (VC), as most of these regions were chosen in a previous study reporting bilateral networks in mice [15]. The connectivity maps were obtained by a correlation analysis, between the averaged BOLD timeseries of the seed region with all voxels in the brain. Correlation analysis was performed using Pearson's correlation, considered standard for FC analyses [30]. The individual connectivity maps were concatenated temporally, and a non-parametric 1-sample t-test was performed, using FSL's *randomise* function [31]. The output of this function is an FWE-Corrected P map, which means it returns P-values with a controlled family-wise error (FWE) rate, corrected for the multiple comparison problem. The final maps were obtained by averaging individual correlation maps, and by thresholding connectivity at a value of 0.2 for the lower resolution runs and 0.15 for high-resolution runs, $p < 0.01$ and a minimum cluster size of 10 voxels. Coincidence maps were also computed with the same thresholds. To evaluate different preprocessing pipelines, an interhemispheric connectivity analysis was conducted, where the correlation between ROIs, anatomically defined in the atlas space in both hemispheres of the brain, was computed. These ROIs were drawn in the same regions that were previously mentioned. Correlation values were then tested with a two-sample two-tailed t-test with unequal variance to check for pairwise significant differences, and a Kruskal-Wallis test, to test for differences of the data distribution.

3. Results

3.1. Optimization of acquisition parameters

Preliminary resting state fMRI acquisitions: functional acquisitions at this stage performed fairly well, although there were some distortions and signal losses typical in EPI sequences. These were attenuated using a two-shot EPI. In Figure 1, raw functional images can be seen. tSNR, which can be used as a data quality index [32][33], was computed as the ratio between temporal mean signal of the brain area, and its standard deviation. The runs exhibited an average tSNR of 29.7 ± 1.2 (mean ± standard deviation of tSNR across animals).

Nyquist ghosts were recurring artifacts throughout the acquisitions, rendering many runs unusable. Following quality control steps, 6 medetomidine runs were considered adequate, and were further analyzed. For the urethane runs, there was only 1 run which was not discarded, and, considering the unsatisfactory results of the medetomidine runs, it was not further processed. Due to the preliminary modest results, urethane acquisitions were ceased, as urethane is a terminal anesthesia. Posterior acquisitions were performed only under medetomidine. An example of a connectivity map with a seed on the primary motor cortex (M1) can be seen in Figure 2.

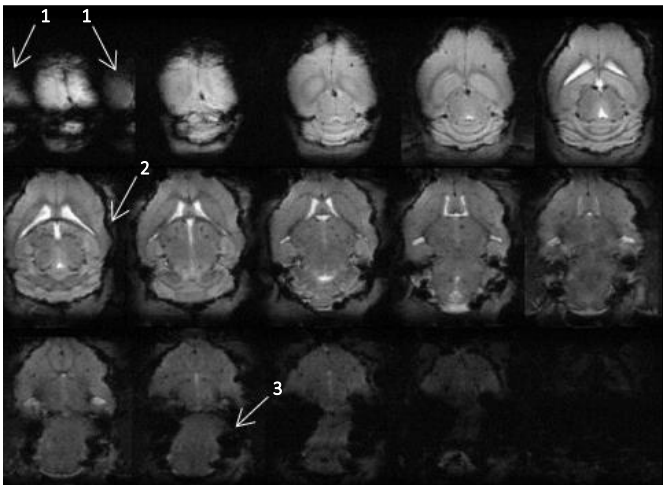

Figure 1: Raw functional images from one representative mouse. Slices presented from dorsal to the ventral part of the brain (from left to right, and top to bottom in the figure). White arrows highlight some of the most evident (1) ghost artifacts, (2) signal losses and (3) distortions.

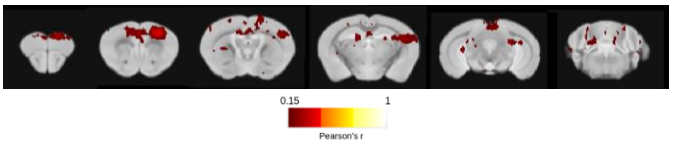

Figure 2: Connectivity map with a seed on M1, using the baseline preprocessing pipeline. 6 individual connectivity maps were averaged, and thresholded at a connectivity of Pearson's r = 0.15. Results are overlaid on the used mouse brain atlas. Slices are shown from rostral to caudal part of the brain, from left to right in the figure.

The other preprocessing pipelines delivered identical results. It is evident that this map is rather noisy, showing apparently random connectivity patterns on most slices, with low correlation values. Slight bilateral signal can be seen in the second slice, but it is not very clean or well defined. On the fourth slice there is also a striped pattern, potentially resembling vasculature.

Urethane characterization: As previously described, two different dosages were tested. Under the 1.2g/kg dosage, both mice were highly unstable throughout the entire session, therefore it was increased to 1.5g/kg. Regarding the 5 mice tested with the latter dosage, it took between 40 to 80 minutes

for them to be stable and cease to spontaneously wake up and/or move. Average temperatures of the mice ranged between 36.45 and 36.72 (standard deviations between 0.09 and 0.24), and average breathing rates ranged from 176 to 221 bpm (standard deviations between 11 and 26).

3.2. Resting state fMRI acquisitions

Functional images were reliable and robust across mice. The lower resolution runs exhibited an average tSNR of 92.7 ± 10.4 (mean ± standard deviation of tSNR across animals). For the high-resolution runs, this value was equal to 53.8 ± 6.3, a foreseeable decrease due to the smaller voxel size. An example of raw functional images can be seen in Figure 3.

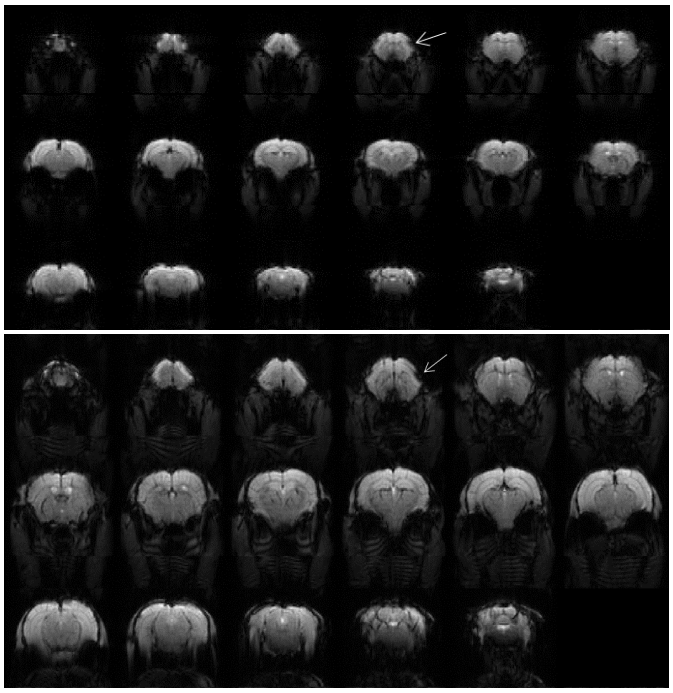

Figure 3: Raw functional images. *(Top):* Low-resolution run and *(Bottom):* High-resolution run. White arrows highlight areas with signal loss.

It can be noticed that these images show much less distortions than the preliminary ones. In both cases, areas with signal losses can be identified, but these are not very severe, and the distortions are quite negligible. Notably, no ghost artifacts were detected. Regarding the tSNR, it should be noted that, since the cryocoil used for signal reception is a surface coil, the measured signal is higher in cortical areas, closer to the coil, than in striatal regions, which results in considerable tSNR variation within the same animal. Animal physiology was verified with visual stimulation runs, and an ROI analysis was performed to ensure suitable preprocessing pipeline performance. After checking resulting individual connectivity maps, these were averaged, and can be observed in Figure 4 and Figure 5. Figure 6 illustrates the positions of the pertinent brain areas that will be subsequently mentioned. Most networks have bilateral signal, although the clusters in the seed's ipsilateral side appear to be slightly larger in some cases, in lower resolution datasets. The difference is clearer in high resolution datasets, where contralateral cluster are visibly smaller. For example, the S1 network has larger clusters on the left side, although it also shows significant connectivity on the right side, even on the lower resolution dataset. Considering the VC network, however, it is possible to see that it is almost symmetrical in the lower resolution datasets, unlike what is seen in high resolution. Despite the mostly bilateral maps, it can be noticed that the Thal seed resulted in a more unilateral map. In the lower resolution dataset, there is a clear lack of clusters in the right side of the brain in this map, and there is a striped pattern that seems to correlate with non-grey matter areas. In the high-resolution dataset, it seems to result in a more spatially restrict map, with some, albeit small, cluster in the contralateral side of the seed. It can also be noticed that the VC network includes part of the anterior cingulate area (ACA) and retrosplenial area (RSP), and that there are some overlapping clusters on M1, S1 and S2 networks. Through visual inspection, it can be noticed that the three pipelines result in quite similar maps. Cluster size varies, but not greatly, and most of the features identified in the maps with baseline processing are recurring across the pipelines. Additionally, some of the smaller clusters are removed with the GSR pipeline. This pipeline also results in a generally smaller cluster size. For example, in M1, S1 and S2 networks, the correlated area is slightly reduced. To further ensure that the final maps were not product of highly variable data, coincidence maps were computed. These present the percentage of times that each voxel had a correlation equal or higher than the used threshold, across runs. Figure 7 shows illustrative coincidence maps for three seeds. As can be observed, these maps are consistent with the corresponding connectivity maps, and this was verified through all seeds and pipelines. Regions showing a high incidence (from 50 to 100%) appear in the final clusters, whereas regions with a low incidence (<50%) do not. However, overall incidence values are slightly lower than in the lower resolution dataset. Finally, an interhemispheric connectivity analysis was carried out, to check for preprocessing pipeline differences, and illustrative results can be found in Figure 8.

A two-sample two-tailed t-test was performed to check for pairwise differences between preprocessing pipelines. For the seven seeds, one significant difference was found between the baseline and the GSR pipeline, for the low-resolution dataset. However, none of the seeds passed the Kruskal-Wallis test, a non-parametric test designed to search for significant differences in the distribution. The mean correlation values found in the boxplots were consistent with the connectivity maps, as most seeds show both high interhemispheric correlation values (from 0.4 to 0.6) and bilateral networks. Accordingly, the most unilateral network, resulting from the thalamus seed, also holds the lowest mean interhemispheric correlation. Interestingly, the thalamic network shows a slightly higher value of mean interhemispheric correlation, compared to the lower resolution dataset, also consistent with the corresponding connectivity map.

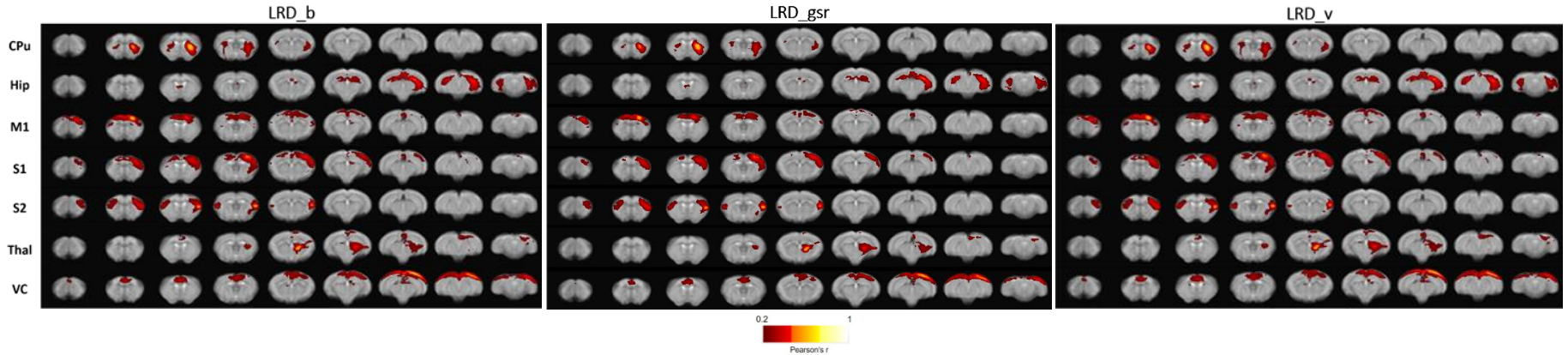

Figure 4: Connectivity maps, averaged from 25 runs from the low-resolution dataset (LRD). Data preprocessed with (Left): the baseline pipeline, (Middle): the GSR pipeline, and (Right): the ventricular signal regression pipeline. 7 seeds were positioned on the left side of Caudate Putamen (CPu), Hippocampus (Hip), Primary Motor Cortex (M1), Primary (S1) and Secondary (S2) Somatosensory cortices, Thalamus (Thal) and Visual Cortices (VC). Thresholds at 0.2 Pearson correlation, $p < 0.01$ and minimum cluster size of 10 voxels. Slices are presented from the rostral part to the caudal part of the brain (from left to right in the figure), and the data is overlaid on top of the averaged functional runs, on the atlas space.

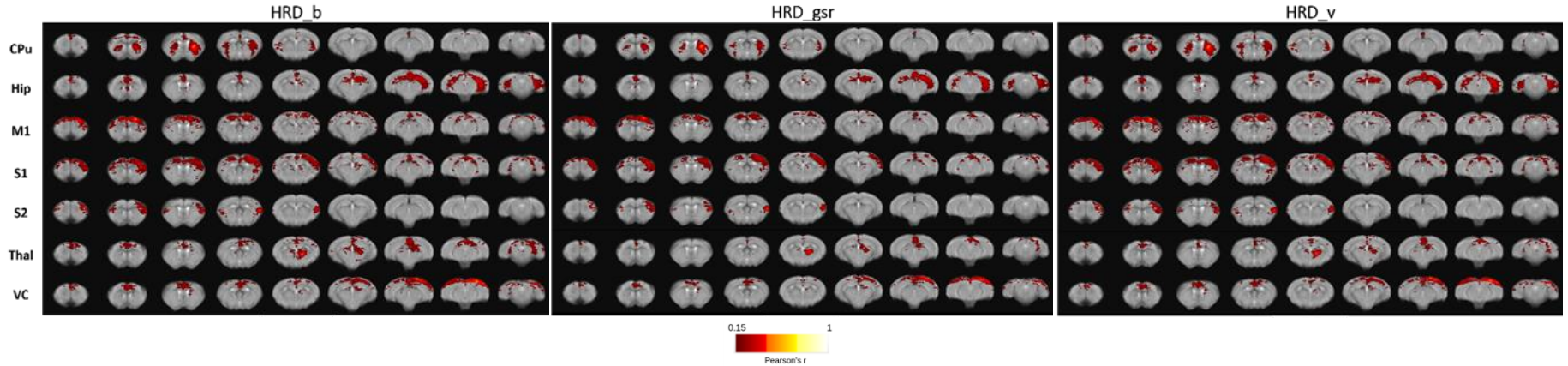

Figure 5: Connectivity maps, averaged from 9 runs from the high-resolution dataset (HRD). Data preprocessed with (Left): the baseline pipeline, (Middle): the GSR pipeline, and (Right): the ventricular signal regression pipeline. 7 seeds were positioned on the left side of Caudate Putamen (CPu), Hippocampus (Hip), Primary Motor Cortex (M1), Primary (S1) and Secondary (S2) Somatosensory cortices, Thalamus (Thal) and Visual Cortices (VC). Thresholds at 0.2 Pearson correlation, $p < 0.01$ and minimum cluster size of 10 voxels.

Figure 6: Anatomical location of pertinent brain areas. For clarity, only the left side of these regions is presented, overlaid on the averaged functional images. ACA = Anterior Cingulate Area, CPu = Caudate Putamen, Hip = Hippocampus, M1 = Primary Motor Cortex, RSP = Retrosplenial Area, S1 = Primary Somatosensory Cortex, S2 = Secondary Somatosensory Cortex, Thal = Thalamus, VC = Visual Cortices.

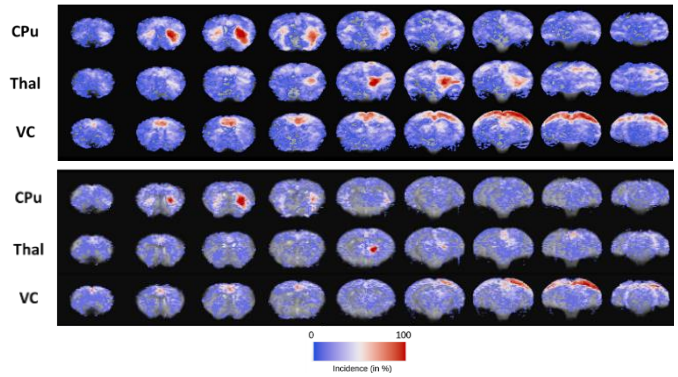

Figure 7: Coincidence map for the baseline preprocessing pipeline. Example for seeds in CPu = Caudate Putamen, Thal = Thalamus, and VC = Visual Cortices. Values of incidence are presented in percentages (blue = low incidence, red = high incidence). (Top): Lower resolution dataset. (Bottom): Higher resolution dataset.

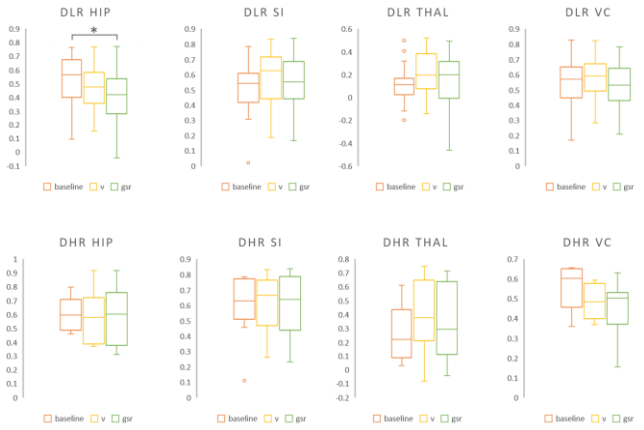

Figure 8: Boxplots showing representative correlation coefficients between 3 interhemispheric regions and 3 preprocessing pipelines. HIP = Hippocampus, SI = Primary somatosensory cortex, THAL = Thalamus, VC = Visual Cortices. In the LR dataset, a vVariation was found between baseline and GSR pipelines, at a significance of $p < 0.05$. The points outside the plots are outliers. (Top): Lower resolution datasets and (Bottom): higher resolution datasets.

4. Discussion

4.1. Optimization of acquisition parameters

Preliminary resting state fMRI acquisitions: The major obstacle encountered in preliminary acquisitions were ghosting artifacts. This issue prevailed on both medetomidine and urethane acquisitions and caused more than half of the runs to be discarded. These might have been caused by eddy currents, induced by the varying magnetic field, which distort the B_0 field, and add phase shifts to the data, creating ghosts in the image, after reconstruction [34]. Reducing phase-encoding resolution could these artifacts, but that was not compatible with the goal of acquiring very high spatial resolution data. Using a single-shot EPI was attempted, as it could have reduced these artifacts as well, but the consequent EPI distortions were too great, rendering the images unusable. Regarding the final connectivity maps, there were not clear and well-defined clusters of correlated areas, and FC was observed only in a very small region adjacent to the seed. The observed stripes could have perhaps originated from vasculature signal that was not removed, and there was not much bilateral signal observed. Even considering only the runs that were not very severely affected by ghosting artifacts, the resolution might have been too high, causing an SNR too low for a rsfMRI experiment. The flip angle (55°) might also have been too low and not allow enough signal to be obtained, compared with the 75° subsequently used, which is closer to the approximate Ernst angle, considering average T_1 values for the mouse brain, and the current TR. Moreover, some functional images had severe distortions, and ultimately, only a small number of runs (6 total) was useable, which might have not provided enough statistical power for a successful network mapping at this resolution.

Regarding the acquisitions under urethane anesthesia, since the mice were fairly stable during the bench testing, a few resting state runs were acquired, as it could help solving some of the previous issues. However, the faster breathing rate is likely to have caused additional animal movement, responsible for an increase of the proportion of runs with ghosting artifacts and runs with a very large number of outliers, resulting in only one usable dataset. Considering the very reduced sample, the small number (3 total) of scanned animals (which is an impactful confounding factor), and that the previous issues (ghosting artifacts and EPI distortions) only seemed to be enlarged, this single run was not further analyzed. Since urethane is a terminal anesthesia, further experiments are advised to be carried out, only after a more robust and high-resolution sequence has been established previously using other anesthetics, and for investigation of structures that are affected by other anesthetic regimes.

Urethane characterization: As could be observed from the bench testing results, breathing and temperature rates were stable for a long time. Despite the results of posterior scanning sessions, it could be observed that the mice were did not wake mid-experiment, unlike in some medetomidine cases, and seemed to be physiologically stable. It could be observed, however, that for this stability to be achieved, the animals must be allowed to stabilize for a long time before the experiments (approximately one hour), since immediately following urethane injection, the mice were still highly reactive, moving and showing signs of wakefulness. Considering the extremely loud noises on the scanner, putting the mice on these circumstances would be both unethical and simply not viable for adequate resting state acquisitions. Higher dosages of urethane can perhaps be tested in the future. Even though fasting the animals prior to the experiment could prove an efficient method for a faster anesthetic effect, it has been shown to alter FC in mice [84]. If further studies using other dosages of urethane should be carried out, it might prove advisable to perform additional measurements on the bench tests, such as partial pressure of oxygen and carbon dioxide, and blood pressure, to further ensure the mouse physiology over time. Overall, although the subsequent acquisitions were not successful, as discussed in

the previous subsection, urethane proved to be a stable anesthetic throughout the sessions, and it might be a viable option in future studies. However, although the ghosting artifacts were not present in posterior experiments, this could still prove to be an issue in further urethane acquisitions.

4.2. Resting state fMRI experiments

Low resolution runs: The lower resolution runs exhibited only minor distortions and no ghosting artifacts. There was a consistent high tSNR throughout the experiments, although it should be noticed that within the same animal there are some variations across the image. The obtained average tSNR values (92.7 and 53.8 for the low- and high-resolution dataset, respectively) are quite good comparing to previous literature, as a tSNR equal of higher to 50 can be considered as suitable [35]. Thus, both low- and high-resolution datasets of the current experiments can be considered to have performed well, especially taking into account that most of the values in the literature were from lower resolution datasets, and that the high tSNR value was mostly constant throughout the experiments.

For these acquisitions, the goal was to follow the protocol established by Nasrallah et al. [15] as closely as possible, in order to reproduce the stable bilateral networks in the current lab. Two more slices could be acquired, comparing to the original study, while keeping the remaining parameters constant, and the anesthesia protocol was changed from an intraperitoneal constant infusion, to a subcutaneous administration. Although this change might alter the time that took for the animals to be sedated, since the absorption rate is slightly slower, subcutaneous administration is simpler and less invasive for the animal, thus being considered a good alternative to intraperitoneal injection. Regarding the overall observed networks, in Figure 4, they were mostly consistent with previous literature. Bilateral networks had already been observed in rats [36], which suggests that these networks are preserved in rodents. Although there had been previous studies where more unilateral networks had been observed in mice [37], several studies have shown ever since that it can be possible to obtain bilateral networks in mice as well [15][38]. This means that in most networks, the connected regions extended beyond the seed and had an approximately equal area on the contralateral side, which is also in accordance with optical imaging findings [39]. The lack of bilateral signal observed in some studies is thought to be due to animal physiology, which is harder to maintain in the mouse, compared with rat. It is also interesting to notice that these bilateral networks are not merely caused by existing structural connectivity. For example, while the left and right S1 are connected via corpus callosum, left and right caudate putamen are not [17], and still show a strong interhemispheric correlation. This is caused by their synchronized activity, which is suggested to reflect communication between regions. However, this communication might not be necessarily direct, as other various inputs (from one or more different regions) might cause their covariance. Thus, it is difficult to infer causality from any of these resting state networks.

Concerning now specific RSNs, it was possible to see that M1, S1 and S2 networks were partly overlapping. Interestingly, these regions had already been shown to be functionally connected, since the first resting state experiment ever performed, in humans [40]. Additionally, some rodent rsfMRI studies performing SBA allowed the mapping of the so-called somatomotor network [41][42], a network englobing the individual motor and somatosensory (M1, S1 and S2) RSNs. ICA studies in mice had already allowed the differentiation of these independent networks [37], with overlaps, as found in this present study. Another consistent finding was the anteroposterior connectivity along the midline, observed in the VC network. It was possible to see that the ACA and RSP were functionally connected to the primary visual cortex, as observed in rats [36] and mice [37].

Despite the good overall results, the thalamic seed only showed ipsilateral functional connectivity. A possible reason for the inconsistency of these results with previous literature can be a misregistration of the functional data, although this hypothesis is unlikely, since the seeds were delineated on top of the averaged functional runs, in the atlas space, and there seemed to be no discrepancies across the runs. A more probable cause for this would be the seed itself, since its specific location, size and shape can have a great impact on the final maps. Different seed sizes were tested, with identical results, but perhaps a combination of these factors could have resulted in the suboptimal mapping of the thalamic network. Partial volume effects should also be considered. The seeds were delineated avoiding transitions between areas, as to minimize PVE, but even slight misregistrations could cause seed region voxels to include signal from unwanted regions. This issue is expected to be less relevant in the higher resolution datasets, due to the lower pixel dimensions. Furthermore, the times of acquisition were not equal for all runs, as they were highly dependent on animal stability in the scanner. Therefore, considering that medetomidine has time-dependent effects on functional connectivity [43], this might have caused some additional variability on the FC patterns of the mice. Lastly, the subcortical location of this region can also be a probable cause for this result, as the inherently lower SNR in these areas could result in more inconstant individual connectivity maps, and a consequent inaccurate averaged map.

Regarding coincidence maps, in Figure 7, they were found to be consistent with connectivity maps, as the areas that survived the thresholding in the connectivity maps show a high coincidence value. Also, they illustrate how noisy the individual datasets are. Almost the entirety of the brain had not null coincidence values. This means that unrelated regions would appear as functionally connected to the seed region, in at least one run. This demonstrates the importance of averaging more animals, to have statistical power for a successful network mapping.

Preprocessing pipelines are a continuous source of debate, in rsfMRI. In this study, three different nuisance removal methods were tested, but no highly significant differences were found. Only one of the 21 pairwise comparisons (or 42, considering comparisons from low- and high-resolution datasets) was found to be significant at a $p < 0.05$, and no difference could be seen in the distribution values. As could be seen in the interhemispheric connectivity boxplots, in Figure 8, individual connectivity values were quite spread, normally ranging from 0.1 to 0.8, with the exception of the Thalamus, which exhibited lower values. No pipeline was found to consistently have higher or lower interhemispheric connectivity than the others, although through visual inspection, and general results, the GSR pipeline seemed to have slightly lower correlation values. This could be expected, since GSR removes a lot of variance in the data, compared with the other nuisance regression alternatives. This also explains why the typical cluster size was smaller in GSR maps. Although interhemispheric analysis is often performed to measure or compare FC patterns “quality”, it should be noted

that a higher correlation value does not always necessarily indicate a better network. As was seen in the ROI analysis, perhaps spurious correlation values can be caused by structured noise, and not by physiological network dynamics. Therefore, these results should be interpreted cautiously, and a visual inspection of the final maps can prove constructive. Besides an interhemispheric correlation analysis and a visual inspection of the data, it is difficult to further investigate differences between pipelines. Since rsfMRI does not have any paradigm, it is difficult to discern if clusters subsequent from either pipeline are indeed belonging to neuronal networks, or mere results from sources of structured noise.

While medetomidine sedation proved to result in overall successful results, a possibly better regime could be attempted, by using a combination of medetomidine and isoflurane, which has already been shown to result in better FC patterns in mice [21]. This was the sedation regime used in the preliminary acquisitions, but perhaps with the established MRI protocol and analysis pipeline, it might have better results in the future. An interesting way to assess pipeline performance could be by comparing the results to those obtained in awake rodents. This was done already in rats [44], instead of the typical interhemispheric correlation analysis done in mice [21]. Awake mice imaging could be an even more interesting path, as anesthesia bias is one of the current major pitfalls of preclinical fMRI studies. Endotracheal intubation and ventilation could be a possible improvement in the case of imaging of anesthetized animals, as it tightly controls the rodent's breathing rate. However, both awake mice imaging and intubation are extremely challenging and time-consuming. Therefore, they would not be likely to be achievable in the time frame of the current project. The use of isoflurane could also be beneficial since, in the present study, the used medetomidine dosage (0.6 mg/kg/h) was found to deliver a very light sedation. This often cause the mice to wake up mid experiment, usually after minimal increases of temperature, and ultimately lead to the session's premature end. This was not consistent with what is described in [15], where it is reported that half of this dosage would result in mice stability up to six hours.

High resolution runs: Similarly to what was found in lower resolution runs, overall results of high-resolution runs were quite positive. The raw data had a very good quality, and despite the high resolution, no ghost artifacts were found. Most findings already described and discussed in the low-resolution runs were also verified in the higher resolution runs. In the connectivity maps, in Figure 5, values of correlation were expected to be lower, due to the decreased tSNR, hence the reduced correlation threshold. This results in slightly "noisier" maps, with a higher number of small clusters, but bilateral networks were still clearly observed, as well as ACA and RSP connectivity along the midline. However, the decreased SNR has clear effects, for example, in the coincidence maps, in Figure 7. It is possible to notice that there is a general decrease of incidence in the connected areas. While it still allows for network detection, it shows that the data is slightly more variable, and not as coherent as the low-resolution data. This is also in agreement with the generally lower correlation values that can be found in the higher resolution dataset, evidenced by the slightly darker colored maps. Analyses at higher resolution will therefore require larger sample sized to overcome the impact of the reduced SNR.

Upon visual inspection, GSR pipeline seems to remove some small significant clusters appearing in the remaining pipelines, and it results in a modest decrease in the size of the largest clusters. However, interhemispheric connectivity analysis, depicted in Figure 8, did not deliver any significant results. Ventricular signal regression seemed to generally result in a slightly higher connectivity across several seeds. This could be since ventricular masks are delineated in very small areas, they can have severe partial volume effects, which are minimized in higher resolutions. Once again, interhemispheric correlation analysis' limitation should be acknowledged, and significant conclusions cannot be made based on such slight differences. An unexpected change was found in the thalamic network, which showed some bilateral connectivity despite this dataset's lower tSNR. This moderate improvement might have been due to an increased spatial specificity, which could cause the vascular effects to be less severe, and possible existing misregistration issues might have been attenuated, since the higher resolution datasets result in a more accurate alignment.

Lastly, considering a possible future project targeted at LC imaging, some factors should be considered. Medetomidine is known to cause a prominent decrease of norepinephrine release and an overall inhibition in the sympathetic nervous system, since it acts mainly on presynaptic receptors in the Locus Coeruleus [45][46]. Thus, different sedation regimes, such as urethane or propofol, should be used. Both anesthetics have been shown to deliver good FC patterns in rodents [44], and suitable cortical interhemispheric connectivity in mice [21]. Another factor that should be taken into account is the slice coverage, as the LC is anatomically positioned ventrally to the beginning of the cerebellum. This coincides with the last slice of most runs in this dataset, but in two of the nine runs, coverage was insufficient for imaging this region. Perhaps a wider coverage could be attempted, either with a higher number of slices, or through an increased slice thickness. The latter option, however, is not recommended, since the current slice thickness is already larger than pixel dimension and can result in significant PVE. A mere shift in the slice coverage could prove sufficient, although in some cases it might compromise the imaging of the beginning of the motor cortex. Finally, when considering the seed-based analysis with the LC as a seed region, perhaps individual seeds should be defined for each individual functional run, and only the resulting connectivity map converted into atlas space. This might allow a more accurate delineation of this small structure, and a thus robust network mapping. To facilitate seed definition, a high-resolution slab covering this region could be acquired, as it would allow direct LC identification. An appropriate contrast should be used, such as T1-weighted MRI with magnetization transfer, based in the neuromelanin content, which has already allowed identification of the LC in mice [47].

In this project, a robust protocol for resting state fMRI in mice, along with a state-of-the-art analysis pipeline has been established. To our knowledge, this is the highest resolution achieved in a resting state functional connectivity study in mice, so far. Although one study has been performed with a 0.1 mm isotropic pixel resolution, no network mapping was performed, and the brain was segmented into larger regions [48], making its effective resolution considerably lower. Overall, the results presented here are promising, although further improvements can be attempted in future studies.

Conclusions and future work

This project was aimed towards the establishment of a robust MRI protocol and an analysis pipeline allowing the mapping of RSNs in mice. More specifically, the goal was to 1) establish a protocol using typical parameters from the literature in the lab

and 2) perform similar experiments at higher resolution to allow the future study of smaller structures. A different anesthetic (urethane) was also tested, as an alternative for medetomidine, which affects the LC noradrenergic system. It was possible to establish and optimize a robust preprocessing pipeline, with three variants, and an analysis pipeline for murine RSN mapping. Bilateral networks were found in both datasets and features consistent with previous literature, especially in the CPu, Hip, M1, S1, S2, and VC. These findings are consistent with previous literature that suggested that RSNs are preserved across rodents [49][14]. A thalamic network could be observed in the higher resolution datasets, but the functionally connected clusters contralateral to seed region was small. Connectivity along the midline was also reported in both datasets, as well as an overlap in the M1, S1 and S2 networks, consistent with previous reports of a somatomotor network. Preprocessing was performed with a baseline pipeline, a GSR variant and ventricular regression variant, but no significant differences were found across pipelines. The baseline pipeline is therefore recommended, as it avoids the additional manual drawing of ventricular masks and the controversy surrounding GSR, respectively. Additionally, urethane was found to deliver a stable and lasting effect on bench tests, but further measurements should be performed before rsfMRI experiments should be carried out with this anesthetic. These are encouraging results and are indicative that even higher resolution could be attempted in the future. Different anesthetics, as well as other FC metrics can also be investigated, such as dynamic FC [50], graph theory [51] or ALFF [48]. Considering the high variability on data acquisition parameters, anesthetic regimes, preprocessing and analysis pipelines used in FC studies, these consistent network mappings are a promising result for rsfMRI in mice as a translational tool for the study of large-scale neural dynamics, as well as the fundamental mechanisms of small structures.

References:

[1] R. M. Birn, “The role of physiological noise in resting-state functional connectivity,” *Neuroimage*, vol. 62, no. 2, pp. 864–870, 2012.

[2] J. Smucny, K. P. Wylie, and J. R. Tregellas, “Functional magnetic resonance imaging of intrinsic brain networks for translational drug discovery,” *Trends Pharmacol. Sci.*, vol. 35, no. 8, pp. 397–403, 2014.

[3] H. Lu and E. A. Stein, “Resting state functional connectivity : Its physiological basis and application in neuropharmacology,” *Neuropharmacology*, vol. 84, pp. 79–89, 2014.

[4] N. Nallasamy and D. Y. Tsao, “Functional Connectivity in the Brain: Effects of Anesthesia,” *Neurosci.*, vol. 17, no. 1, pp. 94–106, Feb. 2011.

[5] K. H. Chuang and F. A. Nasrallah, “Functional networks and network perturbations in rodents,” *Neuroimage*, vol. 163, no. August, pp. 419–436, 2017.

[6] A. M. Belcher *et al.*, “Large-Scale Brain Networks in the Awake , Truly Resting Marmoset Monkey,” vol. 33, no. 42, pp. 16796–16804, 2013.

[7] C. Guedj, E. Monfardini, A. J. Reynaud, A. Farnè, M. Meunier, and F. Hadj-Bouziane, “Boosting Norepinephrine Transmission Triggers Flexible Reconfiguration of Brain Networks at Rest,” *Cereb. Cortex*, vol. 27, no. 10, pp. 4691–4700, Sep. 2016.

[8] X. Huang, Z. Long, and X. Lei, “Electrophysiological signatures of the resting-state fMRI global signal : A simultaneous EEG-fMRI study,” *J. Neurosci. Methods*, vol. 311, no. September 2018, pp. 351–359, 2019.

[9] T.-L. Wu *et al.*, “Intrinsic functional architecture of the non-human primate spinal cord derived from fMRI and electrophysiology,” *Nat. Commun.*, vol. 10, no. 1, p. 1416, 2019.

[10] L. Luo, E. M. Callaway, and K. Svoboda, “Genetic Dissection of Neural Circuits,” *Neuron*, vol. 57, no. 5, pp. 634–660, Mar. 2008.

[11] M. A. Bedell, N. A. Jenkins, and N. G. Copeland, “Mouse models of human disease. Part I: techniques and resources for genetic analysis in mice.,” *Genes Dev.*, vol. 11, no. 1, pp. 1–10, Jan. 1997.

[12] E. Jonckers, D. Shah, J. Hamaide, M. Verhoye, and A. Van der Linden, “The power of using functional fMRI on small rodents to study brain pharmacology and disease,” *Front. Pharmacol.*, vol. 6, p. 231, Oct. 2015.

[13] K. Murphy, R. M. Birn, and P. A. Bandettini, “Resting-state fMRI confounds and cleanup,” *Neuroimage*, vol. 80, pp. 349–359, 2013.

[14] D. N. Guilfoyle *et al.*, “Functional connectivity fMRI in mouse brain at 7T using isoflurane,” *J. Neurosci. Methods*, vol. 214, no. 2, pp. 144–148, Apr. 2013.

[15] F. A. Nasrallah, H. C. Tay, and K. H. Chuang, “Detection of functional connectivity in the resting mouse brain,” *Neuroimage*, vol. 86, pp. 417–424, 2014.

[16] D. Bajic, M. M. Craig, C. R. L. Mongerson, D. Borsook, and L. Becerra, “Identifying rodent resting-state brain networks with independent component analysis,” *Front. Neurosci.*, vol. 11, no. DEC, 2017.

[17] W.-J. Pan, J. C. W. Billings, J. K. Grooms, S. Shakil, and S. D. Keilholz, “Considerations for resting state functional MRI and functional connectivity studies in rodents,” *Front. Neurosci.*, vol. 9, p. 269, Aug. 2015.

[18] S. Bouret and S. J. Sara, “Network reset : a simplified overarching theory of locus coeruleus noradrenaline function,” vol. 28, no. 11, 2005.

[19] S. J. Sara and S. Bouret, “Review Orienting and Reorienting : The Locus Coeruleus Mediates Cognition through Arousal,” *Neuron*, vol. 76, no. 1, pp. 130–141, 2012.

[20] L. A. Schwarz and L. Luo, “Minireview Organization of the Locus Coeruleus-Norepinephrine System,” *Curr. Biol.*, vol. 25, no. 21, pp. R1051–R1056, 2015.

[21] J. Grandjean, A. Schroeter, I. Batata, and M. Rudin, “Optimization of anesthesia protocol for resting-state fMRI in mice based on differential effects of anesthetics on functional connectivity patterns,” *Neuroimage*, vol. 102, no. P2, pp. 838–847, 2014.

[22] C. Baltes, N. Radzwill, S. Bosshard, D. Marek, and M. Rudin, “Micro MRI of the mouse brain using a novel 400 MHz cryogenic quadrature RF probe,” *NMR Biomed.*, vol. 22, no. 8, pp. 834–842, Oct. 2009.

[23] K. J. Friston, *Statistical parametric mapping : the analysis of functional brain images*. Amsterdam; Boston: Elsevier / Academic Press, 2007.

[24] C. Chavarrías, V. García-Vázquez, Y. Alemán-Gómez, P. Montesinos, J. Pascau, and M. Desco, “fMRat: an extension of SPM for a fully automatic analysis of rodent brain functional magnetic resonance series,” *Med. Biol. Eng. Comput.*, vol. 54, no. 5, pp. 743–752, 2016.

[25] B. B. Avants, N. J. Tustison, G. Song, P. A. Cook, A. Klein, and J. C. Gee, “A reproducible evaluation of ANTs similarity metric performance in brain image registration,” *Neuroimage*, vol. 54, no. 3, pp. 2033–2044, Feb. 2011.

[26] K. Gorgolewski *et al.*, “Nipype: a flexible, lightweight and extensible neuroimaging data processing framework in python,” *Front. Neuroinform.*, vol. 5, p. 13, Aug. 2011.

[27] E. Jones, T. Oliphant, and P. Peterson, “SciPy: Open Source Scientific Tools for Python,” Jan. 2001.

[28] A. Roche, “A Four-Dimensional Registration Algorithm With Application to Joint Correction of Motion and Slice Timing in fMRI,” *IEEE Trans. Med. Imaging*, vol. 30, no. 8, pp. 1546–1554, 2011.

[29] A. L. Janke and J. F. P. Ullmann, “Robust methods to create ex vivo minimum deformation atlases for brain mapping,” *Methods*, vol. 73, pp. 18–26, 2015.

[30] J. Bijsterbosch, S. M. Smith, and C. F. Beckmann, *Introduction to Resting State fMRI Functional Connectivity*. 2017.

[31] A. M. Winkler, G. R. Ridgway, M. A. Webster, S. M. Smith, and T. E. Nichols, “Permutation inference for the general linear model,” *Neuroimage*, vol. 92, pp. 381–397, May 2014.

[32] K. H. Chuang *et al.*, “Evaluation of nuisance removal for functional MRI of rodent brain,” *Neuroimage*, vol. 188, no. October 2018, pp. 694–709, 2019.

[33] Y. Ye, Y. Zhuo, R. Xue, and X. J. Zhou, “BOLD fMRI using a modified HASTE sequence,” *Neuroimage*, vol. 49, no. 1, pp. 457–466, Jan. 2010.

[34] M. H. Buonocore and L. Gao, “Ghost artifact reduction for echo planar imaging using image phase correction,” *Magn. Reson. Med.*, vol. 38, no. 1, pp. 89–100, 1997.

[35] J. M. Adamczak, T. D. Farr, J. U. Seehafer, D. Kalthoff, and M. Hoehn, “High field BOLD response to forepaw stimulation in the mouse,” *Neuroimage*, vol. 51, no. 2, pp. 704–712, Jun. 2010.

[36] R. M. Hutchison, S. M. Mirsattari, C. K. Jones, J. S. Gati, and L. S. Leung, “Functional Networks in the Anesthetized Rat Brain Revealed by Independent Component Analysis of Resting-State fMRI,” *J. Neurophysiol.*, vol. 103, no. 6, pp. 3398–3406, Apr. 2010.

[37] E. Jonckers, J. van Audekerke, G. de Visscher, A. van der Linden, and M. Verhoye, “Functional connectivity fMRI of the rodent brain: Comparison of functional connectivity networks in rat and mouse,” *PLoS One*, vol. 6, no. 4, 2011.

[38] F. Sforazzini *et al.*, “Altered functional connectivity networks in acallosal and socially impaired BTBR mice,” *Brain Struct. Funct.*, vol. 221, no. 2, pp. 941–954, 2016.

[39] B. R. White, A. Q. Bauer, A. Z. Snyder, B. L. Schlaggar, J. M. Lee, and J. P. Culver, “Imaging of functional connectivity in the mouse brain,” *PLoS One*, vol. 6, no. 1, 2011.

[40] B. B. Biswal, F. Z. Yetkin, V. M. Haughton, and J. S. Hyde, “Functional connectivity in the motor cortex of resting human brain using echo-planar MRI,” *Magn. Reson. Med.*, 1995.

[41] F. Zhao, T. Zhao, L. Zhou, Q. Wu, and X. Hu, “BOLD study of stimulation-induced neural activity and resting-state connectivity in medetomidine-sedated rat,” *Neuroimage*, vol. 39, no. 1, pp. 248–260, Jan. 2008.

[42] K. A. Williams *et al.*, “Comparison of alpha-chloralose, medetomidine and isoflurane anesthesia for functional connectivity mapping in the rat,” *Magn. Reson. Imaging*, vol. 28, no. 7, pp. 995–1003, Sep. 2010.

[43] M. E. Magnuson, G. J. Thompson, W.-J. Pan, and S. D. Keilholz, “Time-dependent effects of isoflurane and dexmedetomidine on functional connectivity, spectral characteristics, and spatial distribution of spontaneous BOLD fluctuations,” *NMR Biomed.*, vol. 27, no. 3, pp. 291–303, Mar. 2014.

[44] J. Paasonen, P. Stenroos, R. A. Salo, V. Kiviniemi, and O. Gröhn, “Functional connectivity under six anesthesia protocols and the awake condition in rat brain,” *Neuroimage*, vol. 172, no. October 2017, pp. 9–20, 2018.

[45] M. D. Sinclair, “A review of the physiological effects of alpha2-agonists related to the clinical use of medetomidine in small animal practice,” *Can. Vet. J. = La Rev. Vet. Can.*, vol. 44, no. 11, pp. 885–897, Nov. 2003.

[46] T. D. Ambrisko and Y. Hikasa, “Neurohormonal and metabolic effects of medetomidine compared with xylazine in beagle dogs,” *Can. J. Vet. Res.*, vol. 66, no. 1, pp. 42–49, Jan. 2002.

[47] T. Watanabe, Z. Tan, X. Wang, A. Martinez-Hernandez, and J. Frahm, “Magnetic resonance imaging of noradrenergic neurons,” *Brain Struct. Funct.*, vol. 0, no. 0, p. 0, 2019.

[48] T. Tsurugizawa, B. Djemai, and A. Zalesky, “The impact of fasting on resting state brain networks in mice,” *Sci. Rep.*, vol. 9, no. 1, pp. 1–12, 2019.

[49] C. P. Pawela *et al.*, “Resting-state functional connectivity of the rat brain,” *Magn. Reson. Med.*, vol. 59, no. 5, pp. 1021–1029, 2008.

[50] M. G. Preti, T. A. Bolton, and D. Van De Ville, “The dynamic functional connectome: State-of-the-art and perspectives,” *Neuroimage*, vol. 160, no. December 2016, pp. 41–54, 2017.

[51] M. Siyah Mansoory, M. A. Oghabian, A. H. Jafari, and A. Shahbabaie, “Analysis of Resting-State fMRI Topological Graph Theory Properties in Methamphetamine Drug Users Applying Box-Counting Fractal Dimension,” *Basic Clin. Neurosci.*, vol. 8, no. 5, pp. 371–385, 2017.